Advances in Water Resources 188 (2024) 104713

Contents lists available at ScienceDirect

Advances in Water Resources

journal homepage: www.elsevier.com/locate/advwatres

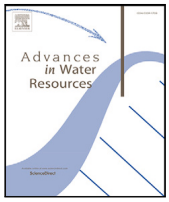

Flood plain inundation modeling with explicit description of land surface macrostructures

Simone Pizzileo, Giovanni Moretti, Stefano Orlandini *

Dipartimento di Ingegneria Enzo Ferrari, Università degli Studi di Modena e Reggio Emilia, Via Pietro Vivarelli 10, Modena, 41125, Italy

ARTICLE INFO

Keywords:
2D flood inundation modeling
Flood plain hydraulic geometry
Macrostructure
Digital surface model
Geomorphologically-informed mesh

ABSTRACT

Although high-resolution digital surface model (DSM) data derived from lidar surveys can describe land surface macrostructures like trees and buildings, digital terrain model (DTM) data obtained by filtering out these macrostructures are commonly used in flood inundation models. In the present study, it is shown for the first time that DSM data can be used directly in flood inundation models by employing automatically-extracted ridges as breaklines for the generation of geomorphologically-informed meshes (GIMs). Even under the simplifying assumption of impermeable macrostructures, especially when GIM refinement is applied, the use of DSM data in preference to DTM data leads to significant improvement in flood predictions. By comparing simulations and observations for a real flood inundation, it is found that the direct use of 1-m DSM data in place of the related DTM data leads to a 42% improvement in predicted flood area, a 36% improvement in predicted flood areal position, and a 25% improvement in predicted times of travel.

1. Introduction

Flood inundations cause billions of dollars of damage and loss of life worldwide (Orlandini et al., 2015; Parker, 2017). To mitigate the adverse impacts of flood inundations, it is essential to understand and predict how inundating flows interact with the Earth's land surface (Merz et al., 2010; Bedient et al., 2013, p. 560; Sanders et al., 2020; Wang et al., 2023). The Earth's land surface is comprised of rocks, soil, vegetation, water bodies, snow, ice, infrastructures, and urban fabrics (Leopold et al., 1964, p. 3; Harvey, 2022, p. 2). Detailed characterizations of the land surface are needed to describe overland and channel flows in drainage basins, river flows, and floodwater propagation over natural and developed flood plains occurring when flow capacity of streams is exceeded or when levees and dams fail (Bates and De Roo, 2000; Horritt and Bates, 2001; Camporese et al., 2010; Dottori et al., 2013; Costabile and Macchione, 2015; Moretti and Orlandini, 2023). Specifically, land surface topography plays an essential role in flood plain inundation modeling (Longley, 2005, p. 4; Yu and Lane, 2006a; Sanders, 2007; Costabile and Macchione, 2015; Medeiros et al., 2022; Moretti and Orlandini, 2023). Land surface topography affects all variables describing surface flows including flow depth, water-surface slope, mean flow velocity and flow discharge (Casas et al., 2006; Azizian and Brocca, 2020). It is relevant to describe both magnitude and timing of these variables in order to determine the interactions between inundating flows with both natural and human-made structures in land planning and emergency management (Yu and Lane, 2006b; Sanders and Mrše, 2007; Tsubaki and Fujita, 2010; Schubert and Sanders, 2012).

Surface flow propagation along fluvial systems and flood plains is commonly described by solving numerically one- or two-dimensional De Saint-Venant unsteady flow governing equations combined with Darcy-Weisbach or Manning-type constitutive equations for resistance to flow (Katul et al., 2002, 2011; Kim et al., 2012). Constitutive equations are essential to quantify friction slope as a function of flow discharge, hydraulic geometry variables, and resistance coefficients (Chow et al., 1988, p. 33; National Academies of Sciences, Engineering, and Medicine, 2024). For the purpose of describing surface flow propagation, the term microtopography can be used to denote land surface features (topographic microstructures) that are not described as part of channel or flood plain hydraulic geometry but rather contributes to resistance coefficients as land surface roughness. Although the term microtopography is often used to denote land surface features having height less than 15 m, the limit between micro and macrotopography (or topographic micro and macrostructures) is clearly smaller for the specific purpose of the present study. High-resolution digital surface model (DSM) data derived from lidar surveys can describe topographic macrostructures like trees and buildings. However, digital terrain model (DTM) data obtained by filtering out these macrostructures are still commonly used in flood inundation models (Sanders, 2007). In existing studies, the effects of natural and human-made topographic macrostructures on surface flow propagation are not described

* Corresponding author.
E-mail addresses: simone.pizzileo@unimore.it (S. Pizzileo), giovanni.moretti@unimore.it (G. Moretti), stefano.orlandini@unimore.it (S. Orlandini).

https://doi.org/10.1016/j.advwatres.2024.104713
Received 26 January 2024; Received in revised form 8 April 2024; Accepted 28 April 2024
Available online 8 May 2024

explicitly from DSM data as part of the land surface hydraulic geometry but rather reconstructed in some way from DTM data or incorporated as part of the land surface roughness contributing to resistance coefficients (Pappenberger et al., 2006; Schubert et al., 2008; Chow, 1959, p. 98; Mays, 2010, p. 113; Brandimarte and Woldeyes, 2013). In order to improve the description of the land surface, Yu and Lane (2006a) suggest that a subgrid refinement of regular computational grids is needed. Liang et al. (2007) proposed to describe buildings in flood inundation models as sponges so that they can absorb floodwater and exercise their effects of floodwater dynamics. Sanders et al. (2008) proposed an integral form of unsteady flow (shallow-water) equations by introducing the concept of anisotropic porosity for urban flood modeling. Sanders et al. (2008) also suggest that the classical unsteady flow equations are suitable to describe surface flow propagation when unstructured meshes are sufficiently detailed to describe land surface macrostructures explicitly. Kim et al. (2015) investigate the errors of models based on the concept of anisotropic porosity which arise from the occurrence of obstacles unevenly distributed in the direction of transverse and longitudinal flows. Alternatively, Guinot et al. (2017) present models where the porosity and flow are described as separate variables for both control volumes and boundaries.

In addition, Tsubaki and Fujita (2010) suggest a classification of land surface macrostructures based on high-resolution DTM data by using wall boundaries for buildings and roughness coefficients for vegetation. Sanders and Mrše (2007), Schubert et al. (2008), and Schubert and Sanders (2012) test four methods for the description of buildings in urban areas, where a building roughness is used, or buildings are represented by altering the original topographic data, or holes in the computational domain are simply used to represent impervious parcels to the flow, or a building porosity is used to estimate a cell-based porosity, and edge-based porosity, and a cell-based frontal area. It is found that some description of land surface macrostructures is essential to reproduce local flow velocities (Schubert and Sanders, 2012). None of the four proposed methods, however, provide an explicit description of land surface macrostructures. Garousi-Nejad et al. (2019) proposed an empirical method based on the height above neighbor drainage (HAND) concept, where synthetic flow rating curves are estimated from high-resolution topographic data and used for mapping, modeling, and predicting flood inundations of urban areas. As pointed out by Ghanghas et al. (2022), however, synthetic flow rating curves are based on the assumption of steady flow and do not reproduce the same effects resulting form the solution of unsteady flow equations with explicit description of land surface micro and macrotopography. Li et al. (2022) find a significant uncertainty associated with models based on the HAND concept. Hocini et al. (2021), Chaudhuri et al. (2021), and Aristizabal et al. (2023) propose alternative solutions to reduce these uncertainties.

A special effort is made to incorporate the information content of high-resolution topographic data into 2D hydrodynamic models (Marks and Bates, 2000; Mason et al., 2003; Begnudelli and Sanders, 2007; Schubert et al., 2008; Garousi-Nejad et al., 2019). Existing studies highlight that uncertainty in the elevation of macrostructures such as vegetation, buildings, levees, and other human-made structures significantly affect simulation results (e.g., Hocini et al., 2021). Bates et al. (2003) explicitly express the need for methods to identify and connect linear topographic features in high-resolution topographic data. Especially in lowlands, delineating blockage and overtopping elements such as levees and flood walls is found to be essential to obtain reliable flood hazard assessments (Kahl et al., 2022). The LANDMARK algorithm developed by Moretti and Orlandini (2023) is particularly useful to describe flow barriers in flood inundation modeling. This algorithm automatically extracts ridge networks from high-resolution topographic data in a geomorphologically-meaningful manner without altering the original topographic data. Selected elements of the ridge network can be used as breaklines to generate geomorphologically-informed meshes (GIMs) having a greater potential than geomorphologically-uniformed meshes (GUMs) to preserve the detail of high-resolution topographic data only where it is relevant to flood inundation modeling (Moretti and Orlandini, 2023). The capability of LANDMARK to describe explicitly land surface macrostructures from DSM data, however, has not been tested so far. In facts, there is significant potential for improving existing 2D flood inundation models by applying novel terrain analysis methods to DSM data. Three research questions arise. First, can high-resolution DSM data be used to describe explicitly trees and buildings in 2D flood inundation models? Second, can advanced terrain analysis methods provide suitable GIMs for the explicit description of trees and buildings in 2D flood inundation models? Third, what is the improvement brought by the use of DSM data in preference to DTM data in terms of predicted flood area, flow depth, and times of travel of inundations?

In the present study, these three research questions are addressed by using high-resolution DSM data, advanced terrain analysis methods, and suitable flood inundation models. Land surface macrotopography is loosely defined as topographic variability on a scale that can be described by high-resolution topographic data and existing terrain analysis methods. Macrotopography is assumed to describe land surface macrostructures like trees and buildings having a prominence greater than or equal to 0.25 m. Microtopography encompasses topographic structures having a prominence less than 0.25 m and land surface roughness. Under this light, the modeling strategy investigated in the present study make use of all the information content of high-resolution DSM data to describe explicitly the land surface macrostructures, by leaving to flow resistance coefficients the role to describe the effects of all topographic microstructures that are not captured by topographic data. The LANDMARK algorithm developed by Moretti and Orlandini (2023) is used to extract automatically the ridge network from DSM data. Unstructured meshes that adapt to selected ridges (GIMs) are then generated within the HEC-RAS 2D flood inundation model to describe explicitly topographic macrostructures as part of the land surface hydraulic geometry. With respect to the existing methods, DSM data are used in preference to DTM data, and GIM refinement is applied in preference to GUM refinement. Innovative terrain analysis methods coupled with the HEC-RAS 2D flood inundation model are described in Section 2 by referring to a real flood inundation occurred in northern Italy in 2020. The simulation of this flood inundation is compared with observations in Section 3. Results are discussed in Section 4 and conclusions are synthesized in Section 5.

2. Materials and methods

2.1. Study area and flood inundation event

The geographical area of the Po River valley located in northern Italy on the right-hand side of the Panaro River near the town of Modena is considered to be a representative example of a lowland terrain markedly shaped by natural and human-made topographic structures. Part of the considered area is shown in Fig. 1. In the morning of 6 December 2020, the right-hand side levee of the Panaro River located between the towns of Gaggio and Bagazzano (44°39′6.4″N, 10°59′01.2″E) failed and the surrounding areas were inundated (Figs. 1a and 1b). The levee failure occurred during a flood event generated by rainfall, rainfall-on-snow, and snowmelt in the 890-km^2 drainage basin contributing to the flood control reservoir located in San Cesario. More precisely, from 4 December 2020, 199 mm of precipitation fell on Panaro River drainage basin and the progressive increase in temperature caused a snowmelt of about 20 mm. The water-surface elevation of the San Cesario flood control reservoir rose rapidly reaching the maximum of 39.96 m asl (above sea level) on 6 December 2020 at 3:45. The flood hydrograph released by the flood control reservoir caused the levee failure on 6 December 2020 at 6:30 (supporting information, Figs. S1–S3). About 8×10^6 m^3 of floodwater spilled out of the riverbed by spreading over the surrounding rural and urban areas.

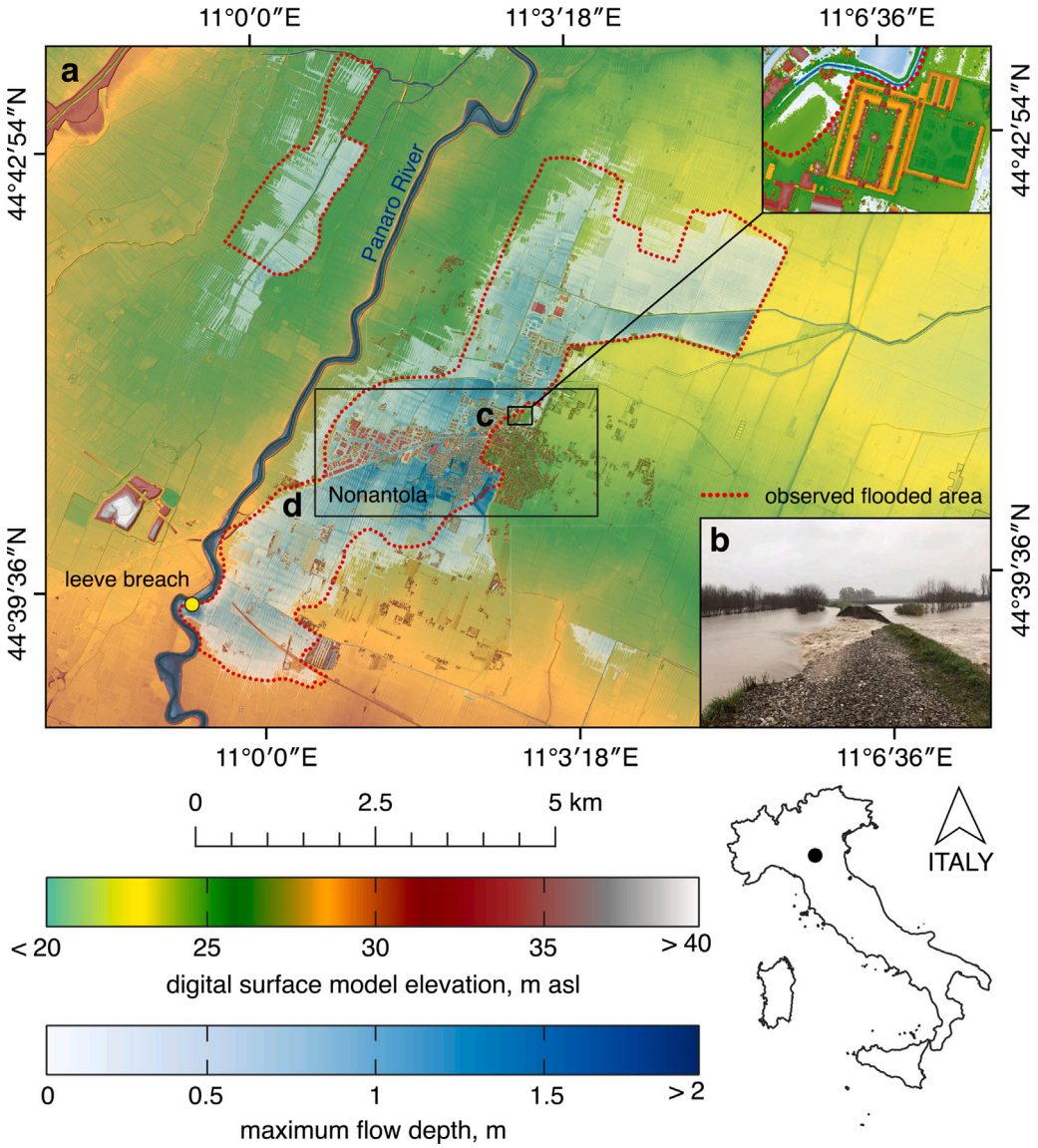

Fig. 1. Planimetric view of the study area and of the considered flood inundation event. (a) Simulated flood areas are represented by blue shades. Observed flood areas are those bounded by the red dotted line. The levee failure occurred on 6 December 2020 is shown in inset b (courtesy of "Agenzia Interregionale per il fiume Po"). Land surface topography is described by a 1-m digital surface model (DSM). Inset c is also used in Fig. 3. Inset d including the town of Nonantola is used in Fig. 4.

Due to the natural slope of the land, the floodwater spread in a North-East direction and reached the town of Nonantola in a few hours. The failed levee was repaired within 24 h by limiting the flood area to 18.07 km^2.

2.2. Data sources

The high-resolution topographic data used in the present study were generated from point clouds obtained through lidar surveys. A first lidar survey was carried out by the Italian "Ministero dell'Ambiente, della Tutela del Territorio e del Mare" (Rome, Italy) in 2008 for most of the study area (Fig. 1). A second lidar survey was carried out by the "Agenzia Interregionale per il fiume Po" (Parma, Italy) in 2015 for the Panaro River extending upstream to the flood control reservoir located in San Cesario. A third lidar survey was carried out by the "Agenzia Interregionale per il fiume Po" (Parma, Italy) in 2017 for the lowland lying on the right-hand side of the Panaro River. From point clouds, DSM and DTM data are generated as sketched in Fig. 2 for rural (Fig. 2a) and urban (Fig. 2b) areas. A DSM is an elevation model that captures both the environment natural (Fig. 2a) and artificial (Fig. 2b) features. A DSM describes the elevation of the top reflective surfaces. A DTM is bare earth elevation model. A DTM is often obtained from the DSM by filtering out topographic macrostructures like trees and buildings (Petrie and Kennie, 1987; Guth, 2006). A 1-m DSM and the corresponding DTM obtained by filtering out trees and buildings are available for the study area (Fig. 1). The elevation profile within the selected computational domain spans from 2.9 to 52.3 m asl, with an average elevation of 25.7 m asl. The point density in the surveys is greater than 1.5 points/m^2. The corresponding DTM exhibits a vertical accuracy not greater than 15 cm and a planimetric accuracy not greater than 30 cm (Di Martire et al., 2017).

The Italian Fire Department conducted a thorough survey to delineate the extents of inundated zones (Fig. 1). The acquired data were used to evaluate flood inundation models. River stage and flow data were available for the considered flood event. Stage hydrographs immediately upstream and downstream the San Cesario flood control reservoir were used to determine the released flow hydrograph during the flood event from experimental reservoir outflow characteristic relationships. This flow hydrograph gives the upstream (Neumann) boundary condition for the flood wave propagating along the Panaro River (supporting information, Fig. S1). Other stage hydrographs

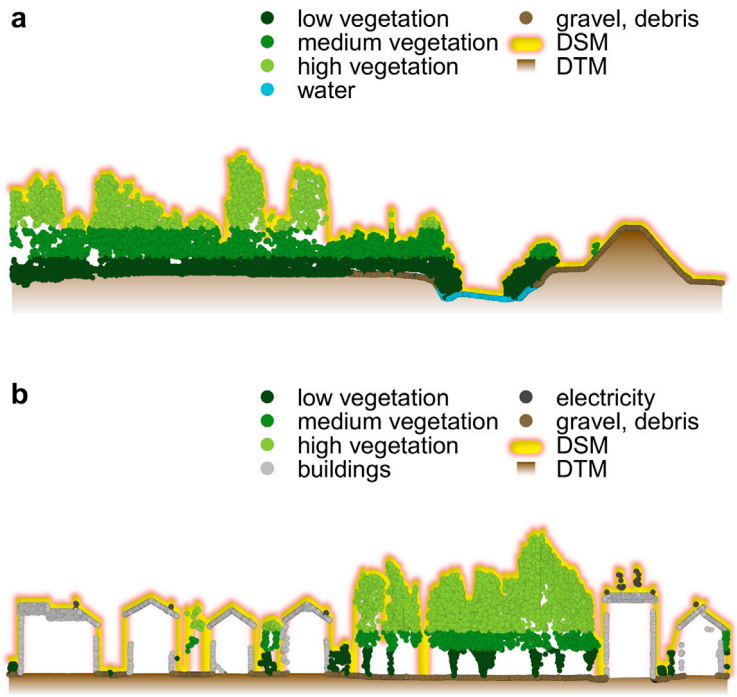

Fig. 2. Explicit description of land surface macrostructures as given by a digital surface model (DSM) in (a) rural and (b) urban areas. Point clouds are often obtained from a lidar survey. The digital terrain model (DTM) is often obtained from the DSM by filtering out macrotopographic structures like trees and buildings.

and related uniform flow rating curves were used for the stations of Navicello, Bomporto, and Bondeno to give the downstream boundary condition for the flood wave and to corroborate results obtained from a riverflow propagation model (supporting information, Figs. S2 and S3). A (Cauchy) downstream boundary condition was assigned in the present study by using the uniform flow rating curve at the station of Bondeno. The validated flood wave propagation model was used to estimate the flow hydrograph released by the levee to the surrounding rural and urban areas.

2.3. Land surface characterization

The 1-m DSM is used to describe land surface macrostructures over an area of 847.88 km^2. This area is shown in part in Fig. 1. The areal extension of vegetation canopies is 44.92 km^2 (5.3%), the areal extension of buildings is 102.64 km^2 (12.1%), and the areal extension of the remaining land surface is 700.32 km^2 (82.6%). The land surface area that is not covered by vegetation canopies or buildings is covered by short vegetation (601.11 km^2, 70.9%) or infrastructures (99.21 km^2, 11.7%). The vegetation canopy height, as determined from the difference between DSM and DTM data, ranges from 1.87 to 30.31 m and has an average value of 14.09 m. The short vegetation height, as determined from the difference between DSM and DTM data, ranges from 0.00 to 0.38 m and has an average value of 0.04 m. Land surface macrostructures such as trees and buildings are not filtered out, but rather incorporated in flood inundation models as part of the flood plain hydraulic geometry. An attempt to describe explicitly land surface macrostructures from DSM data is made under the simplifying assumption that macrostructures are impermeable. No attempts are made, for instance, to reproduce storage and flow across vegetation canopies and buildings. When land surface macrostructures described by DSM data are filtered out and the obtained DTM data are used in flood inundation models, trees and buildings are considered to be completely permeable by floodwater and flow resistance coefficients are used to also represent the blocking effects due to these macrostructures. In facts, vegetation canopies and buildings are not completely permeable nor impermeable, and specific efforts are needed to determine the hydraulic permeability of these macrostructures. The present study just compares with observations flood simulations where land surface macrostructures are described explicitly from DSM data as impermeable obstacles and flood simulations where land surface macrostructures are filtered out and DTM data are used in combination with flow resistance coefficients also representing the blocking effects due to macrostructures. The assumption of permeable macrostructures will be explored in future studies as a next logical step.

To obtain accurate and efficient simulations of flood inundations, ridges (lines of intersection at the top between opposite slopes) identifying in particular land surface macrostructures are extracted from DSM data, and unstructured computational meshes adapting to the extracted ridges are used. These meshes are denoted in the present study as GIMs (geomorphologically-informed meshes), as opposed to GUMs (geomorphologically-uninformed meshes) where mesh elements do not necessarily adapt to extracted ridges. GIM generation and refinement is therefore supported by the extraction of ridge networks at the desired level of detail. GUM generation and refinement, instead, is just based on the definition of the planar domain and of refinement regions within this planar domain. Ridge networks are extracted from DSM data in a fully-automated manner by using the LANDMARK algorithm described in Moretti and Orlandini (2023). High-resolution topographic data are not altered. Neither coarsening nor depression filling is applied. Depressions and nested systems of endorheic and exorheic basins are rather handled by the LANDMARK algorithm. In this way, trees and buildings are incorporated in the land surface characterization as they result from the lidar survey of the highest reflective surface. The impact of DSM data is evaluated by also considering the related DTM data obtained by filtering out trees and buildings. In both cases, the obtained ridge networks are used as bases for the determination of GIMs as shown in Fig. 3. The use of DSM data is reported in Figs. 3a and 3b, whereas the use of DTM data is reported in Figs. 3c and 3d. Ridge networks at different levels of detail are extracted by setting a critical dispersal area for ridge network representation S_c (Moretti and Orlandini, 2023). A further threshold is introduced then to select along the extracted ridge networks only those ridges that display a prominence with respect to the average elevation of the terrain in the dispersal area greater

than or equal to a threshold value P_t (Moretti and Orlandini, 2023). In Fig. 3, the level of detail with which the ridge network is represented is selected by setting S_c equal to 10 m^2 (Figs. 3a and 3c) and 5×10^5 m^2 (Figs. 3b and 3d), and P_t always equal to 0.25 m. The extracted ridges are used as breaklines to identify relevant surface flow barriers, and unstructured meshes are generated in such a way that mesh cell edges adapt perfectly to these breaklines so that the profile of land surface macrostructures given by DSM data is perfectly assimilated along mesh cell edges.

GIMs are obtained by using the domain boundary and the ridge network as breaklines. A breakline is a line used to connect data representing a distinct land surface feature, like a domain boundary, a ridgeline, or a flowline of a ditch or stream. The mesh generator included in the Hydrologic Engineering Center's (HEC) River Analysis System (RAS) developed by the US Army Corps of Engineers is used in the present study (Hydrologic Engineering Center, 2016, 2022). Breaklines are incorporated by the HEC-RAS mesh generator in accordance with an assigned point spacing. When a breakline is defined, the HEC-RAS mesh generator seeks a Voronoi tessellation that follows the breakline by placing polygon edges coincident with the breakline segments. This ensures that the features in the land surface are accurately depicted in the computational mesh by forcing cell faces to have the elevation values of the ridges observed in DSM data. Far from assigned breaklines the Voronoi tessellation is unconstrained and therefore gives a regular mesh. Results obtained from the HEC-RAS mesh generator are generally satisfactory and can be made as accurate as desired by applying some mesh refinement in points when Voronoi polygons edges are not found to adapt perfectly to the assigned breaklines. The problem of determining the optimal Voronoi tessellation that adapts to assigned ridge networks is beyond the scope of the present study, but certainly deserves to be addressed in a future specific research effort. It is remarked that ridges and breaklines can in principle be identified and incorporated in HEC-RAS 2D independently from LANDMARK, but in practice this process becomes a prohibitive task without LANDMARK as the level of mesh refinement increases.

Six different scenarios of GIMs generated from DSM data are considered as shown in Fig. 4. GIMs are obtained by setting S_c equal to 10, 10^2, 10^3, 10^4, 10^5, and 10^6 m^2 and P_t always equal to 0.25 m (Fig. 4a, 4b, 4c, 4d, 4e, and 4f, respectively). Unstructured computational meshes are composed of elements having size ranging from about 5 m × 5 m to 200 m × 200 m. The number of cells depends on the number of assigned breaklines. In the case of the most detailed unstructured mesh (S_c = 10 m^2, P_t = 0.25 m, Fig. 4a), 2642 breaklines and 173,268 mesh elements are obtained. With a 5-m regular grid the number of grid cells would be about 34×10^6, which is up to 200,000 times higher than in unstructured meshes, with clear implications on model efficiency. In addition, mesh elements of the unstructured mesh better adapt to extracted ridges than cells of a regular grid having fixed orientation. The modeling strategy adopted in the present study distills in a geomorphologically-meaningful manner the detail offered by DSM data in such a way that the topographic detail is maximum where it is needed and it is relaxed where it is not essential. Unstructured meshes are evaluated in the present study by combining the use of DSM and DTM data as well as GIM and GUM refinement as reported in

Table 1. In both the cases in which DSM and DTM data are used, the parent GUM is set equal to the parent GIM obtained by setting S_c = 10^6 m^2 and P_t = 0.25 m (case 1 in Table 1). From these parent cases, GIM and GUM refinements are applied by resulting in refined meshes exhibiting the numbers of cells reported in Table 1 (cases 2–6). The use of the obtained unstructured meshes in flood inundation modeling is described in Section 2.4.

Table 1
Number of cells in geomorphologically-informed meshes (GIMs) and geomorphologically-uninformed meshes (GUMs) generated from DSM and DTM data.

Case	S_c (m^2)[a]	Number of cells			
		DSM data		DTM data	
		GIM	GUM	GIM	GUM
1	10^6	162,521	162,521	157,899	157,899
2	10^5	163,793	163,419	158,991	159,101
3	10^4	166,589	166,870	159,789	159,533
4	10^3	170,183	170,269	161,562	161,753
5	10^2	171,438	171,309	162,768	162,714
6	10^1	173,268	173,423	164,091	163,872

[a] The specification of S_c is relevant to the generation of GIMs (cases 1–6) and of the parent GUMs (case 1, which are set equal to the related parent GIMs). P_t = 0.25 m in all cases. LANDMARK and related parameters S_c and P_t are not used in GUM refinement (cases 2–6), which is applied by assigning refinement regions to the parent GUMs (case 1).

2.4. Flood plain inundation modeling

Flood plain inundation modeling with explicit description of land surface macrostructures is investigated in the present study by combining the HEC-RAS 2D flood inundation model and the LANDMARK algorithm for the extraction of ridge networks from high-resolution DSM data (Hydrologic Engineering Center, 2016; Moretti and Orlandini, 2023). The HEC-RAS 2D flood inundation model solves numerically the 2D unsteady flow equations also known as shallow-water equations (Hydrologic Engineering Center, 2020b, chapter 6, p. 3). The HEC-RAS 2D "full momentum" solver (Eulerian–Lagrangian Method) is used in the present study. Key ridges, encompassing levees, roads, railway embankments, and land surface macrostructures are automatically identified from 1-m DSM data using the LANDMARK algorithm (Section 2.3). Ridges extracted by the LANDMARK algorithm are configured as breaklines in HEC-RAS 2D and act as barriers to flow along the mesh element faces. Land surface macrostructures described by the 1-m DSM are fully assimilated by HEC-RAS 2D along the faces of mesh elements only. Macrostructures that are not aligned with the mesh element faces solely influence the distribution of surface water storage within the mesh elements. The impact of land surface macrostructures on surface water storage within the mesh elements is described approximately when macrostructures are filtered out or assumed to be impermeable, and needs to be investigated in future studies by using permeable macrostructures. Resistance to flow is described in HEC-RAS 2D flood inundation models by assigning a value of the Manning resistance coefficient n to each land use class identified in the study area and by eventually performing some calibration. Eight land use classes are identified in the study area and initial values of n are assigned to each class by following the recommendations given in the HEC-RAS 2D manual (Hydrologic Engineering Center, 2020a, p. 21). The final values of n obtained for each land use class after calibration are reported in Table 2. Different distributions of the Manning resistance coefficient n are used in combination with DSM and DTM data to differentiate the case where land surface macrostructures are described explicitly and n is only used to represent the effects of microstructures from the case where land surface macrostructures are filtered out and n is used to represent the effects of both micro and macrostructures (supporting information, Fig. S4). Manning's n are assigned by HEC-RAS 2D to each mesh cell face by using the value of the underlying land use class in the face midpoint. Examples of extracted breaklines and obtained flood inundation maps at the single-house scale are shown in Fig. 5 for the DSM-based model with the finest GIM (S_c = 10 m^2, 173,268 cells, Figs. 5a and 5b) and the DTM-based model with the finest GIM (S_c = 10 m^2, 164,091 cells, Figs. 5c and 5d). The more realistic flow paths and waterlogging shown in Fig. 5b is directly connected to the ability of DSM data and GIM refinement to identify the geometry of buildings. Ridges used as breaklines in Fig. 5 are parts of open tree networks as expected from the LANDMARK algorithm.

Conventional performance metrics such as false alarm ratio (FAR), critical success index (CSI), and probability of detection (POD), as well as error functions such as mean error (ME), mean absolute error (MAE),

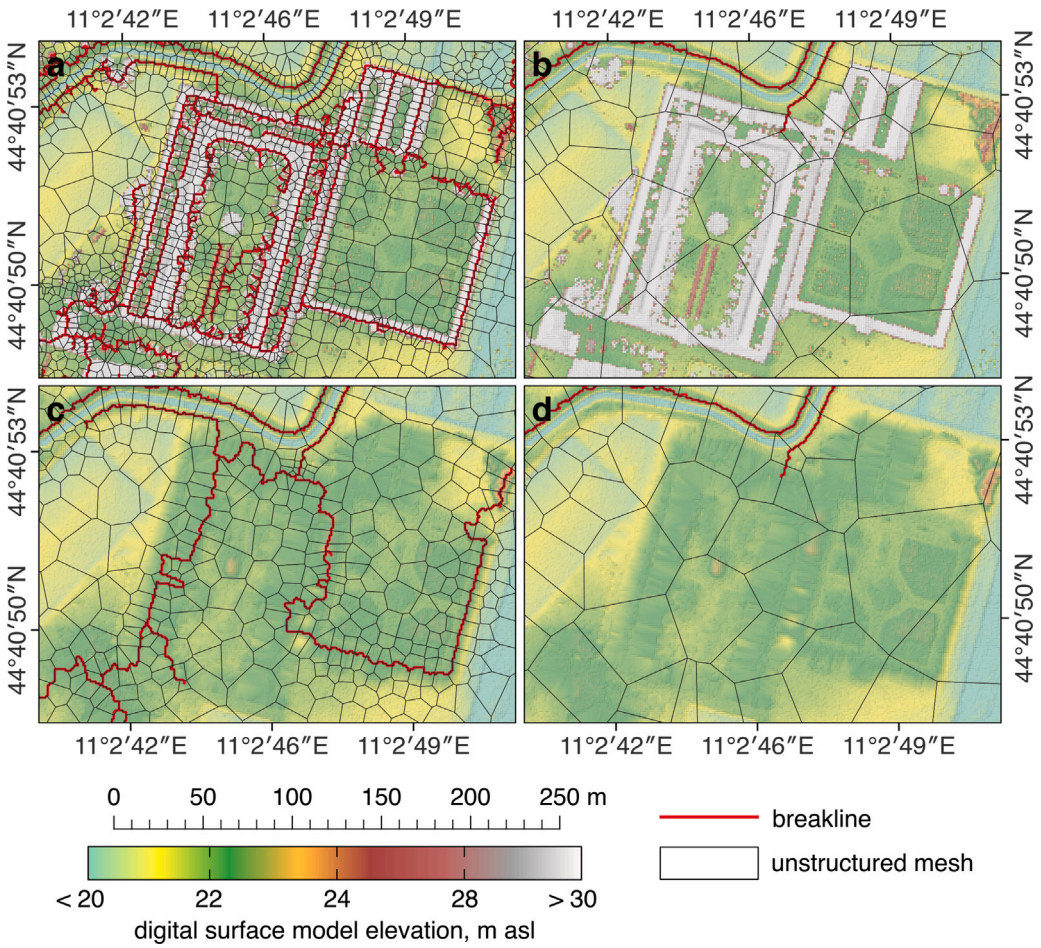

Fig. 3. Geomorphologically-informed meshes (GIMs) in the inset c of Fig. 1 obtained from (a and b) digital surface model (DSM) data and (c and d) digital terrain model (DTM) data. Ridges are extracted using LANDMARK by setting S_c equal to (a and c) 10 m^2 and (b and d) 5×10^5 m^2 and P_t always equal to 0.25 m. Extracted ridges are used as breaklines in HEC-RAS 2D and GIMs are generated in such a way that mesh cell edges adapt perfectly to breaklines.

Table 2
Land uses and related Manning's resistance coefficients.

Land use	Manning's n (s m$^{-1/3}$)	
	DSM-based model	DTM-based model
Panaro River	0.038	0.038
Flood Plains	0.082	0.082
Poor Vegetated Rural Area	0.060	0.065
High Vegetated Rural Area	0.060	0.080
Industrial Urban Area	0.060	0.140
Downtown Urban Area	0.060	0.160
Oldtown Urban Area	0.060	0.180
Drainage Network	0.025	0.025

root mean square error (RMSE), volume conservation error e_V, type-1 error, and type-2 error are used to evaluate flood inundation models. By considering simulated and observed flood areas as shown, for instance, in Fig. 6 for event described in Section 2.1, three different areas can be distinguished: (1) area denoted as true positive TP, which marks the flood area that is simulated and observed; (2) area denoted as FP, which marks the flood area that is simulated but not observed; and (3) area denoted as false negative FN, which marks the flood area that is observed but not simulated. It is specified that the observed flood area (FN + TP) is assumed to include the footprint of topographic macrostructures like trees and buildings as these structures are normally flooded internally. Areas TP, FP, and FN make it possible to define the quantities FAR, CSI, and POD as

$$\mathrm{FAR} = \frac{\mathrm{FP}}{\mathrm{TP}+\mathrm{FP}}, \tag{1}$$

$$\mathrm{CSI} = \frac{\mathrm{TP}}{\mathrm{TP}+\mathrm{FN}+\mathrm{FP}}, \tag{2}$$

and

$$\mathrm{POD} = \frac{\mathrm{TP}}{\mathrm{TP}+\mathrm{FN}}, \tag{3}$$

respectively. The FAR given by Eq. (1) is a verification measure of categorical forecast performance equal to the number of false alarms (FP) divided by the total number of event forecasts (TP + FP). The CSI given by Eq. (2), also called the threat score, is a verification measure of categorical forecast performance equal to the total number of correct forecasts (hits, TP) divided by the total number of forecasts plus the number of misses (hits + misses + false alarms, TP + FN + FP). The POD given by Eq. (3) is a verification measure of categorical forecast performance equal to the total number of correct event forecasts (hits, TP) divided by the total number of events observed (TP + FN). The perfect forecast gives a FAR equal to 0, a CSI equal to 1, and a POD equal to 1. Type-1 error E_1 accounts for the absolute difference between observed and simulated flood areas independently of their positions, and is expressed as

$$E_1 = \frac{|\mathrm{FN}-\mathrm{FP}|}{\mathrm{FN}+\mathrm{TP}}. \tag{4}$$

Type-2 error E_2 accounts for the nonoverlapping area, and is expressed as

$$E_2 = \frac{\mathrm{FN}+\mathrm{FP}}{\mathrm{FN}+\mathrm{TP}}. \tag{5}$$

Type-1 error given by Eq. (4) is an indicator of the difference between simulated and observed flood areas regardless of the relative position

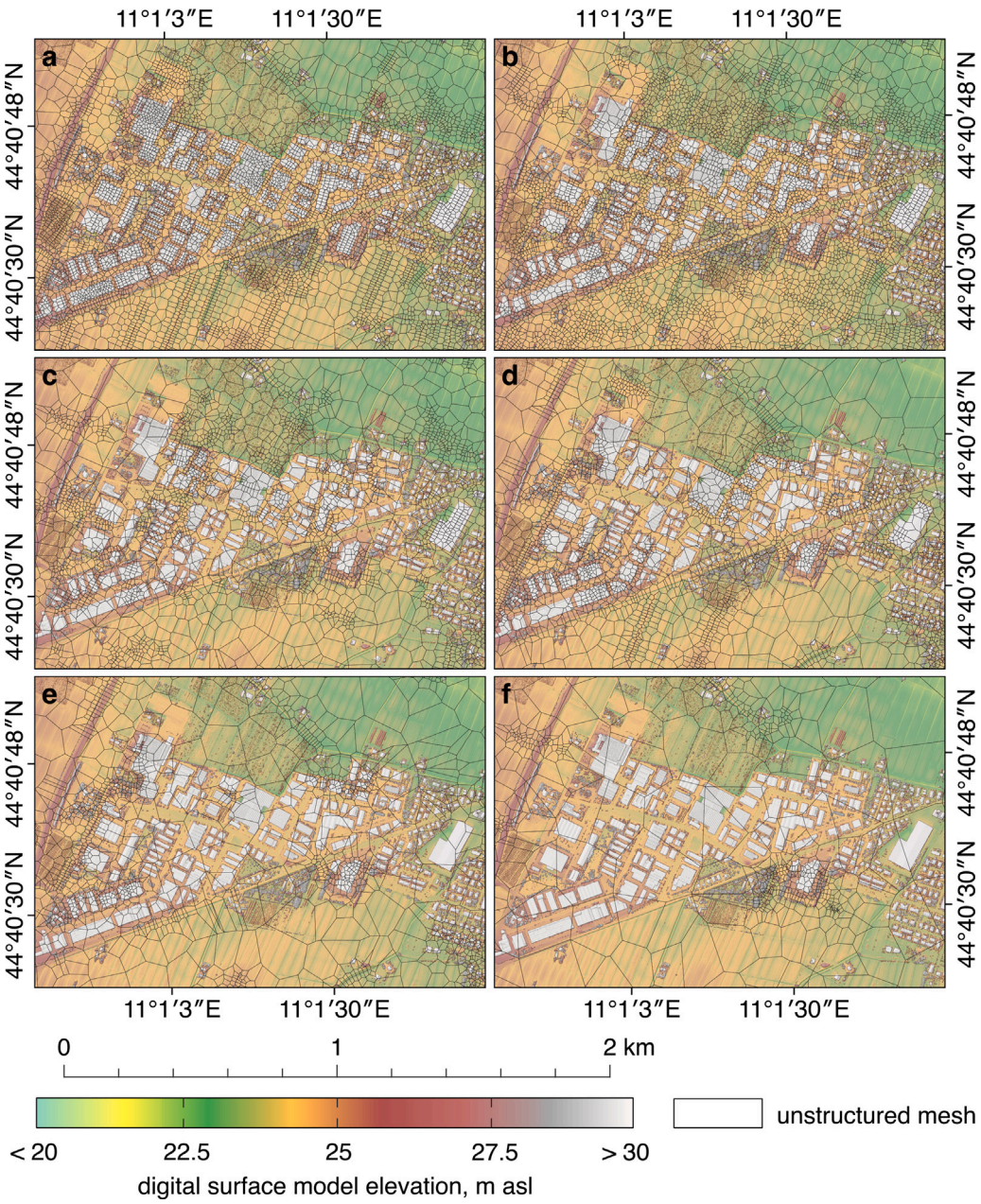

Fig. 4. Geomorphologically-informed meshes (GIMs) in the inset d of Fig. 1 obtained from digital surface model (DSM) data and different detail in the description of the land surface. Ridges are extracted by using LANDMARK with S_c equal to (a) 10, (b) 10^2, (c) 10^3, (d) 10^4, (e) 10^5, and (f) 10^6 m^2 and P_t always equal to 0.25 m. Detail increases as S_c decreases.

of these areas (Moretti and Orlandini, 2008). On the other hand, type-2 error given by Eq. (5) also accounts for the different areal position of simulated and observed flood areas (Moretti and Orlandini, 2008). As FN $\geq$ 0, TP $\geq$ 0, and FP $\geq$ 0, the occurrence E_1 equal to 0 implies that simulated and observed flood areas have the same magnitude but not necessarily the same areal position, whereas E_2 equal to 0 implies that simulated and observed flood areas have the same magnitude and areal position, namely a perfect overlap between the simulated and observed flood areas.

Flood inundation models with GIM and GUM refinements exhibiting similar number of cells are compared in Fig. 7 in terms of (a) FAR, (b) CSI, and (c) POD. From the parent case of a GIM with 162,521 cells obtained by setting $S_c = 10^6$ m^2 (case 1 in Table 1), refined GIM are obtained by decreasing the values of S_c (cases 2–6 in Table 1). The related numbers of cells are 163,793, 166,589, 170,183, 171,438, and 173,268, respectively. Correspondingly, refined GUM are obtained from the same parent case to obtain approximately the same numbers of cells (163,419, 166,870, 170,269, 171,309, and 173,423, respectively, in Table 1). For the numerical analysis of flood inundation models, FAR, CSI, and POD are computed with respect to the most detailed solution obtained for a GIM with $S_c = 10$ m^2 (173,268 cells), and not with respect to observations are indicated in Fig. 6. FAR, CSI, and POD are found to display comparable values with GUM refinement, indicating that the HEC-RAS 2D "full momentum" solver is numerically stable with respect to mesh refinement. Flood inundation model performance are found to increase with GIM refinement as a result of the improved ability of GIMs to describe the land surface topography as given by DSM data. Simulation results change with mesh refinement as a result of the change in the topographic characterization of a complex land surface. The analysis reported in Fig. 7 indicates at the same time the independence of simulations from GUM refinement (as expected from the HEC-RAS 2D "full momentum" solver) and the improvement of

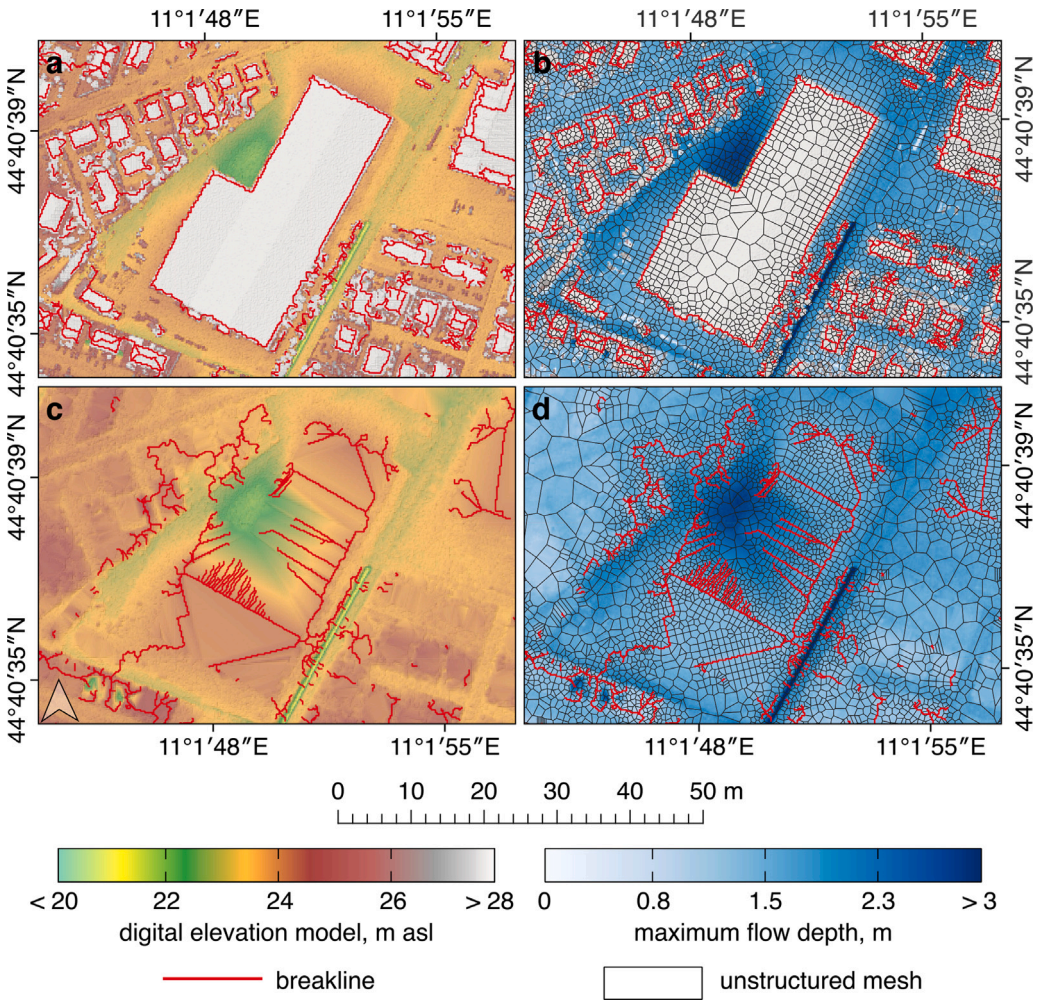

Fig. 5. Extracted ridges used as breaklines (a and c) and flood inundation maps (b and d) at a single-house scale for (a and b) the DSM-based model with the finest GIM (S_c = 10 m^2, 173,268 cells) and (c and d) the DTM-based model with the finest GIM (S_c = 10 m^2, 164,091 cells).

results with GIM refinement (as expected from the LANDMARK ability to accurately describe the land surface). Mesh refinement has little impact on simulation results if it is not supported by the introduction of geomorphologically-informed breaklines at the subgrid scale.

The numerical convergence of the HEC-RAS 2D "full momentum" solver with respect to changes in time step is documented in Fig. 8. Flood inundation models with the finest GIM (173,268 cells in Fig. 2) and different time steps ($\Delta t = 1, 5, 10, 30, 60$ s) are compared in Fig. 8 in terms of (a) FAR, (b) CSI, and (c) POD. For the numerical analysis of flood inundation models, FAR, CSI, and POD are computed with respect to the most detailed solution obtained for $\Delta t = 1$ s, and not with respect to observations are indicated in Fig. 6. Although the obtained FAR, CSI, and POD display increasing or decreasing trend, the range of plotted quantities indicate that flood inundation models exhibit comparable performances across the considered time steps. ME, MAE, RMSE, and e_V are computed with respect to the most detailed solution obtained for $\Delta t = 1$ s. The obtained value of ME, MAE, and RMSE are satisfactory (supporting information, Fig. S5). Volume conservation error e_V exhibits values on the order of 10^{-4} for $\Delta t \leq 30$ s, and on the order of 10^{-2} for $\Delta t = 60$ s, which is anyway acceptable (supporting information, Fig. S6). The numerical experiments reported above indicate that the developed HEC-RAS 2D flood inundation models ensure stable results with respect to (geomorphologically-uninformed) mesh refinement and time step selection.

3. Results

HEC-RAS 2D flood inundation models with explicit description of land surface macrostructures based on DSM data and GIM generation are evaluated by comparing simulations and observations for the real flood inundation event described in Section 2.1. Results obtained from the proposed modeling strategy are compared to those obtained by using DTM data where trees and buildings are filtered out. In addition, GIM refinement is compared to GUM refinement. All cases reported in Table 1 are considered. Flood inundation models are evaluated in terms of flood areas, water-surface elevation, and flood times of travel. Simulations start from 5 December 2020 at 00:00 and end on 8 December 2020 at 24:00. A computational time interval of 1 min is used. The breach begins on 6 December 2020 at 6:30 and has a duration of about 5 h by reaching a maximum length of about 70 m. During these 5 h, a linear progression of the breach is assumed. The breach was subsequently repaired in 24 h. For simulating a 4-day flood event with the most detailed unstructured mesh (S_c = 10 m^2, 173,268 cells, and 2,642 breaklines) with a laptop having an Intel® Core™ i9–11900H @ 4.9 GHz CPU and 64 GB RAM, a wall-clock time of 29 min 8 s is needed.

Simulated and observed flood areas are compared in terms of FAR, CSI, and POD across GIMs and GUMs exhibiting variable numbers of cells for both DSM-based and DTM-based flood inundation models as reported in Fig. 9. Even under the simplifying assumption of impermeable macrostructures, especially when GIM refinement is applied,

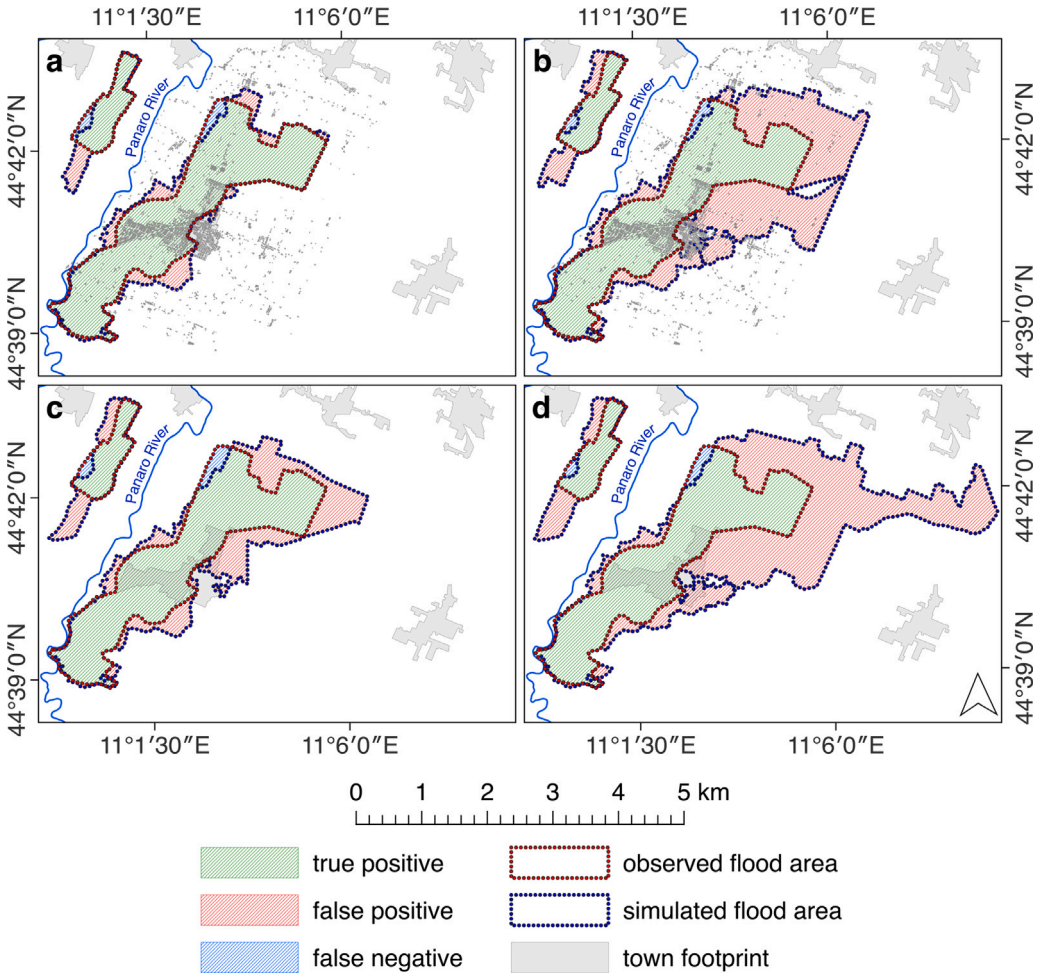

Fig. 6. Comparison between simulated and observed flood areas. True positive (TP), false positive (FP), and false negative (FN) are filled in green, red, and blue respectively, for (a) finest simulation based on DSM data and $S_c = 10$ m^2, (b) coarsest simulation based on DSM data and $S_c = 10^6$ m^2, (c) finest simulation based on DTM data and $S_c = 10$ m^2, and (d) coarsest simulation based on DTM data and $S_c = 10^6$ m^2.

the use of DSM data in preference to DTM data leads to significant improvement in flood predictions. Simulated and observed flood areas are also compared in terms of type-1 and type-2 errors in Figs. 10. Figs. 10a and 10b show the values of E_1 and E_2, respectively, for each of the six simulated scenarios shown in Figs. 4a–4f and for the six corresponding scenarios in which DTM data are used in place of DSM data, where in all cases the critical dispersal area for ridge network representation S_c varies. One can note that using DSM data in preference to DTM data for the generation of the unstructured meshes leads to significant decreases in type-1 error E_1 (42% for $S_c = 10$ m^2 in Fig. 10a) and in type-2 error E_2 (36% for $S_c = 10$ m^2 in Fig. 10b) for $S_c < 10^4$ m^2, whereas it leads to an increase of E_1 and E_2 (6% for $S_c = 10^6$ m^2 in Figs. 10a and 10b) for $S_c \geq 10^4$ m^2.

Fig. 11 shows the spatial distribution of time of travel for the six scenarios introduced in Fig. 4. When the unstructured meshes having a fine resolution are used ($S_c = 10, 10^2$, and 10^3 m^2 in Figs. 11a, 11b and 11c, respectively), surface water spreads slowly, causing the northern area of Nonantola to be flooded in a time of travel of about 7 h after the levee failure. In contrast, when unstructured meshes having coarse resolution are used ($S_c = 10^4, 10^5$, and 10^6 m^2 in Figs. 11d, 11e, and 11f, respectively), flood inundation times of travel as small as 2 h are obtained, especially in the transition between the center of Nonantola and the northern rural area. In addition, observed and simulated times of arrival for the real flood inundation event considered in this study indicate that the use of DSM data in preference to DTM data leads to significant improvement in the prediction of times of travel (supporting information, Fig. S7 and Tab. S1). Fig. 12 shows the location of three transects (A, B, and C) crossing both rural and urban areas around the town of Nonantola. Profiles of DSM data along these three transects are reported in the insect of Fig. 12. Transects A, B, and C in Fig. 12 display different relative positions of rural and urban areas along the direction of propagation of the flood inundation. Land surface profile along the transect A displays a sparsely urbanized terrain followed by a rural terrain. Land surface profile along the transect B displays a densely urbanized terrain followed by a rural terrain. Land surface profile along the transect C displays a rural terrain followed by a sparsely urbanized terrain. The simulated water-surface elevations along the three selected transects (A, B, and C) shown in Fig. 12 by considering DSM-based and DTM-based unstructured meshes are compared in Fig. 13 by dividing each transect into three portions.

4. Discussion

Two innovations are explored in the present study. First, DSM data are used in preference to DTM data to explicitly describe land surface macrostructures like trees and buildings. Second, the detail offered by high-resolution DSM data is distilled in a fully-automated and geomorphologically-meaningful manner by applying the LANDMARK algorithm for the extraction of relevant ridges (those displaying $P \geq P_t$, where in the present study $P_t = 0.25$ m) at different levels of detail in the representation of the ridge network (as determined by $S \geq S_c$). The extracted ridges are used as breaklines in the HEC-RAS

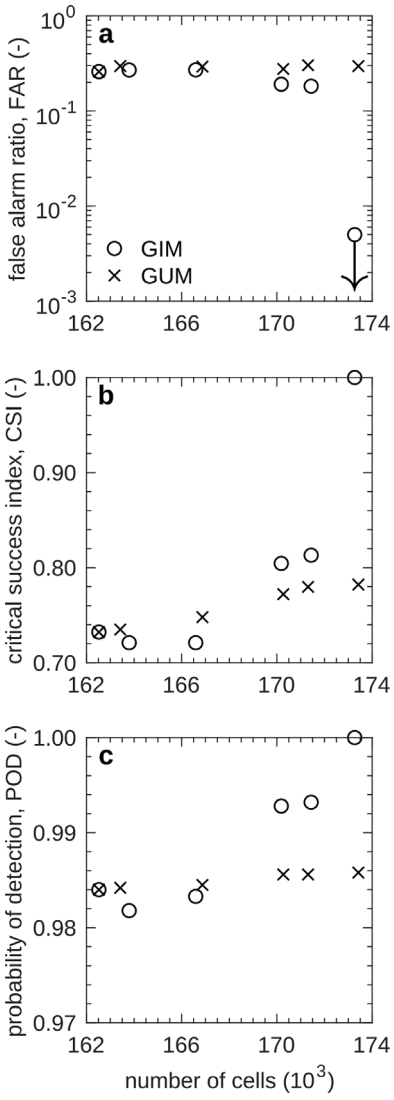

Fig. 7. Comparison between flood inundation models with geomorphologically-informed mesh (GIM) and geomorphologically-uninformed mesh (GUM) refinements having similar number of cells in terms of (a) false alarm ratio FAR, (b) critical success index CSI, and (c) probability of detection POD. FAR, CSI, and POD are computed with respect to the most detailed solution obtained for a GIM with $S_c = 10$ m^2 (173,268 cells).

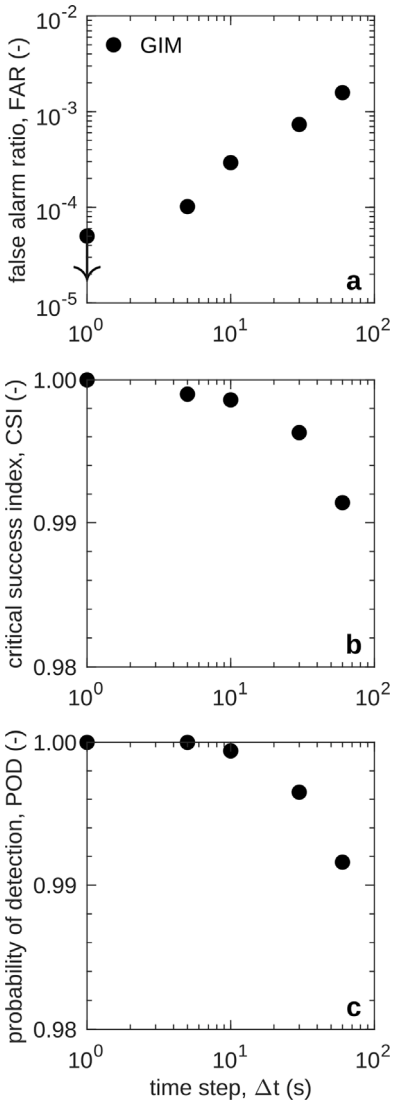

Fig. 8. Evaluation of flood inundation models with the finest geomorphologically-informed mesh (GIM, 173,268 cells) in terms of (a) false alarm ratio FAR, (b) critical success index CSI, and (c) probability of detection POD, for different time steps ($\Delta t = 1, 5, 10, 30, 60$ s). FAR, CSI, and POD are computed with respect to the most detailed solution obtained for $\Delta t = 1$ s.

2D flood inundation model so that the topography observed in high-resolution DSM data is fully assimilated along the cell edges of the generated unstructured meshes with clear benefits to model accuracy. The impact of the resulting GIMs on flood inundation modeling is evaluated by comparing simulated and observed flood areas, over four modeling strategies obtained by combining DSM and DTM data as well as GIM and GUM refinements. It is remarked that the innovation in the combined use of LANDMARK and HEC-RAS 2D is not just a simple use of observed ridges as breaklines, which can even be performed manually, but rather the ability of LANDMARK to fully penetrate high-resolution topographic data for extracting ridges at any desired level of detailed through the selection of appropriate parameters S_c and P_t, which is a prohibitive task without LANDMARK. The analysis carried out applies to any flood inundation model that makes the same smart use of high-resolution topographic data as HEC-RAS 2D.

The ability of a flood inundation model based on 1-m DSM data to reconstruct a real flood inundation event is shown in Fig. 1. The zoom made into inset c shows how trees and buildings are captured by high-resolution DSM data. As illustrated in Fig. 2, compared to the more traditional use of DTM data, DSM data describe explicitly land surface macrostructures like trees, embankments, and buildings, which can be extracted as ridges by the LANDMARK algorithm and incorporated in HEC-RAS 2D as breaklines. As shown in Fig. 3, breaklines obtained from DSM data and the LANDMARK algorithm with $S_c = 10$ m^2 and $P_t = 0.25$ m are sufficiently detailed to capture the topography of trees and buildings (Fig. 3a), whereas breaklines obtained by setting $S_c = 5 \times 10^5$ m^2 and $P_t = 0.25$ m do not entirely capture topographic macrostructures observed in DSM data (Fig. 3b). Breaklines obtained from DTM data and the LANDMARK algorithm with $S_c = 10$ m^2 and $P_t = 0.25$ m capture the planar position of trees and buildings that were filtered out but left some track on DTM data (Fig. 3c), whereas breaklines obtained by setting $S_c = 5 \times 10^5$ m^2 and $P_t = 0.25$ m do not capture topographic macrostructures observed in DSM data (Fig. 3d).

The use of DSM data and GIMs in flood inundation modeling, as compared to the use of DTM data and GUMs, is evaluated by considering cases exhibiting different levels of detail (numbers of cells) as shown in Fig. 4 for DSM data and GIMs and reported in Table 1 for all possible combinations. Flood inundation maps shown, for instance, in Fig. 5 reveal that the combined use of DSM data, GIMs

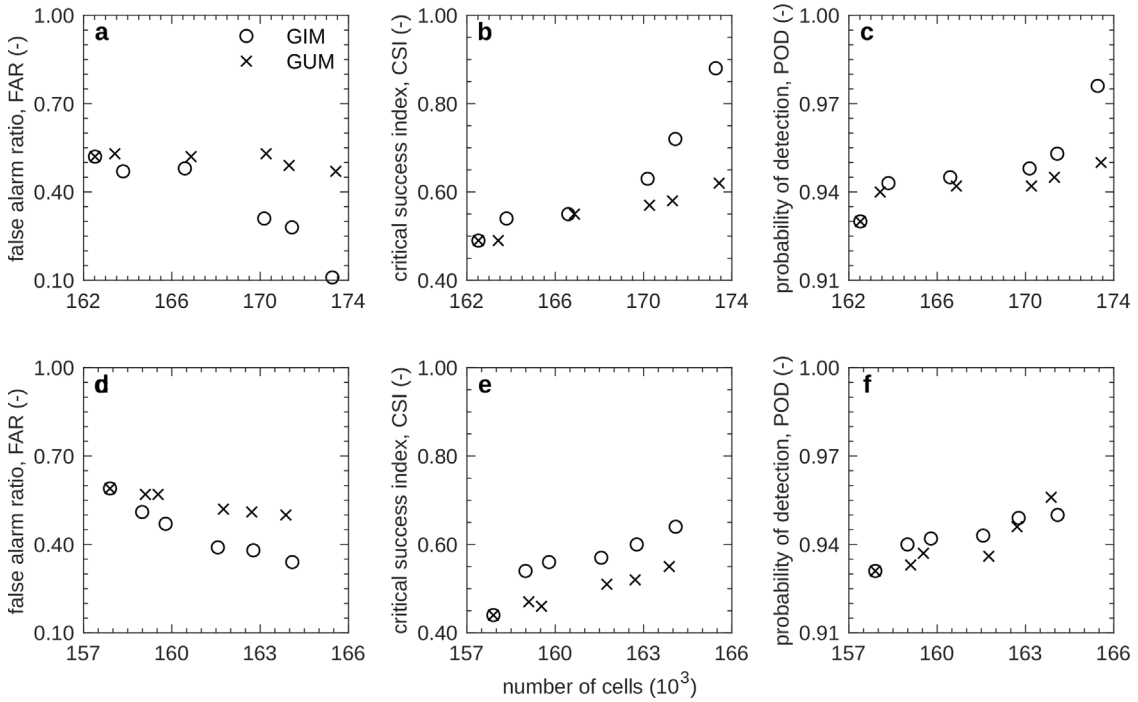

Fig. 9. Comparison between flood inundation models with geomorphologically-informed mesh (GIM) and geomorphologically-uninformed mesh (GUM) refinements having similar number of cells in terms of (a) false alarm ratio FAR, (b) critical success index CSI, and (c) probability of detection POD. DSM-based models are considered in plots (a–c) and DTM-based models are considered in plots (d–f). FAR, CSI, and POD are computed by considering simulated and observed flood areas.

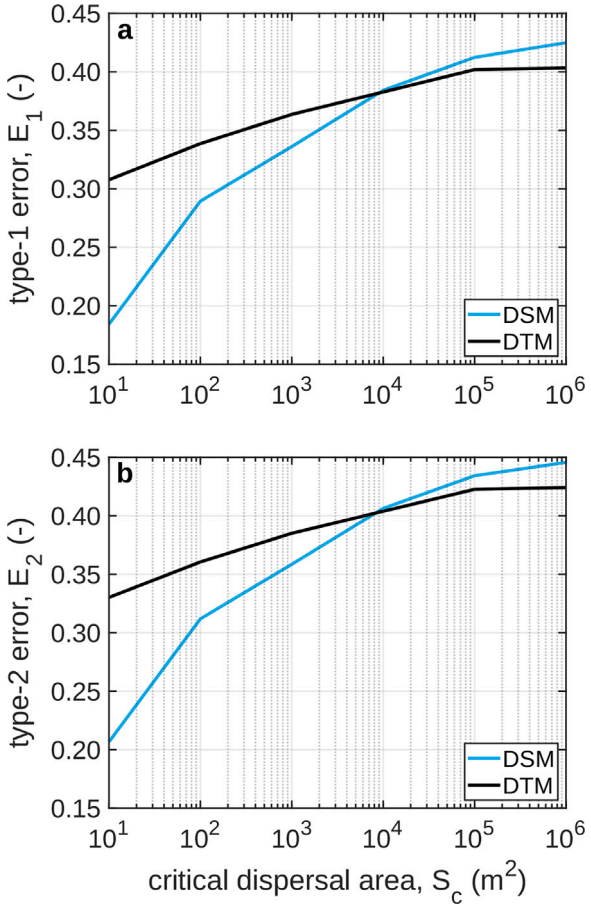

Fig. 10. Type-1 and type-2 errors (Eqs. (4) and (5), respectively) in the prediction of flood areas obtained by comparing surface flow simulations based on digital terrain model (DTM) or digital surface model (DSM) data and observations, for different levels of detail in the description of the land surface. Detail increases as S_c decreases.

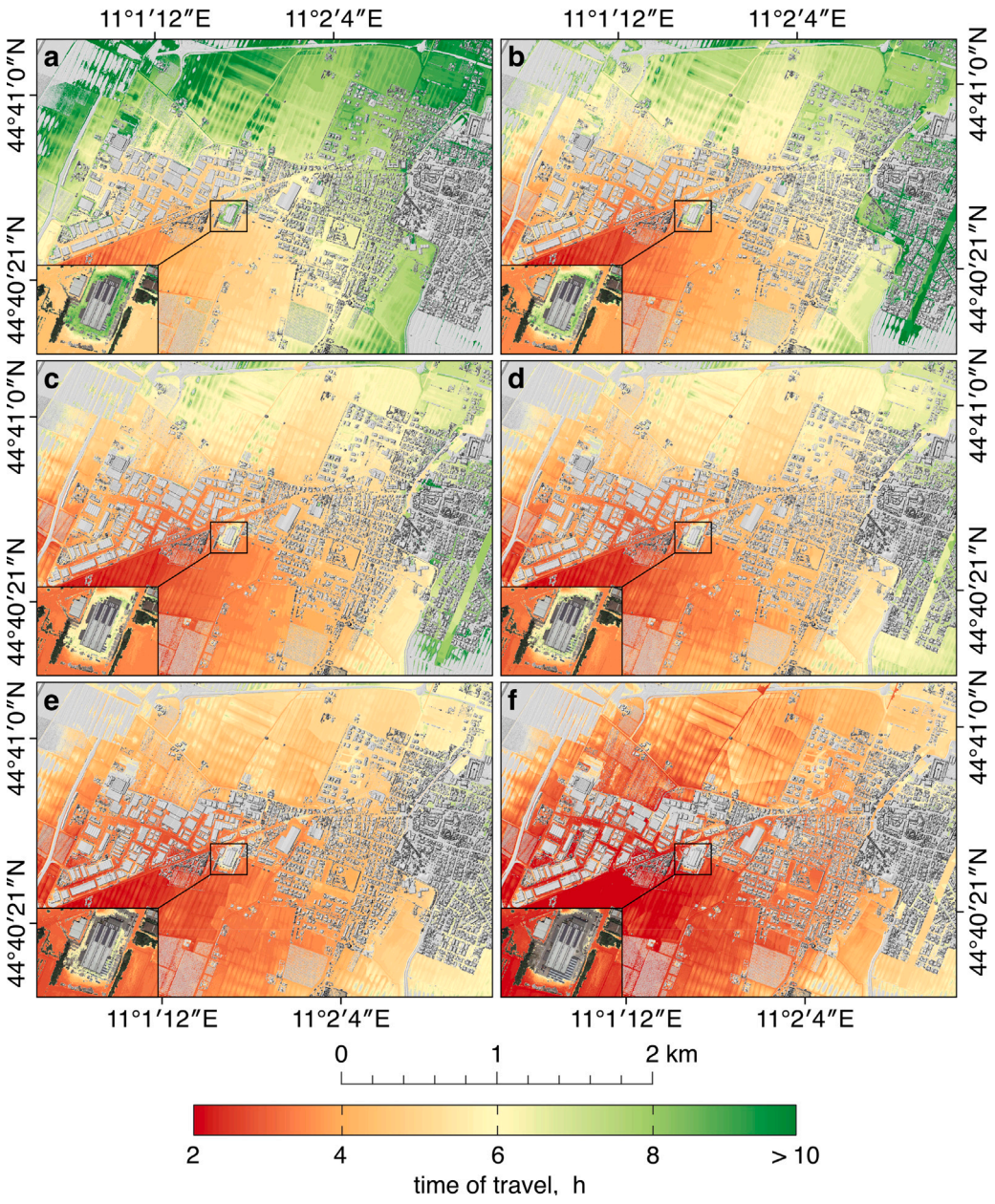

Fig. 11. Time of travel of the flood inundation in the inset d of Fig. 1 as obtained from digital surface model (DSM) data and different detail in the description of the land surface. Ridges are extracted by using LANDMARK with S_c equal to (a) 10, (b) 10^2, (c) 10^3, (d) 10^4, (e) 10^5, and (f) 10^6 m^2 and P_t always equal to 0.25 m. Detail increases as S_c decreases.

obtained from LANDMARK, and HEC-RAS 2D makes it possible the explicit description of land surface macrostructures in flood inundation modeling by producing accurate inundation maps at the single-house scale. A comprehensive analysis is obtained by comparing simulated and observed flood areas in all the cases reported in Table 1 in terms of FAR, CSI, and POD, on the basis of TP, FP, and FN determinations illustrated, for instance, in Fig. 6. The results of the analysis are shown in Fig. 9. Starting from parent case 1 in Table 1 ($S_c = 10^6$ m^2, 162,521 and 157,899 cells for DSM and DTM data, respectively), where the GIM and the GUM are exactly the same, GIM refinement is found to improve performance metrics significantly more than GUM refinement. Differences in performance metrics are especially relevant when the level of detail (number of cells) increases and DSM data are used. FAR is found to decrease significantly when DSM data are used and GIM refinement is applied (Fig. 9a). This significant decrease is not observed when DTM data or GUM refinement are used (Figs. 9a and 9d). The obtained results indicate that FP flood areas are significantly reduced by the combined use of DSM data and GIM refinement. CSI is found to increase significantly when DSM data are used and GIM refinement is applied (Fig. 9b). This significant increase is not observed when DTM data or GUM refinement are used (Figs. 9b and 9e). The obtained results indicate that FN and FP flood areas are significantly reduced by the combined use of DSM data and GIM refinement. POD is found to provide relatively stable results in all cases (Figs. 9c and 9f). The obtained results indicate that FN flood areas play a relatively minor role in the observed flood inundation event. The impact of GIM refinement over GUM refinement is relatively less important when DTM data are used because the capabilities of LANDMARK remain relatively unexpressed where macrostructures are filtered out. In light of the results reported in Fig. 9, it seems that the simplifying assumption of impermeable macrostructures does not cause important artifacts in the description of ground surfaces with short vegetation or flow across sparse trees like those observed in the study area (Section 2.3).

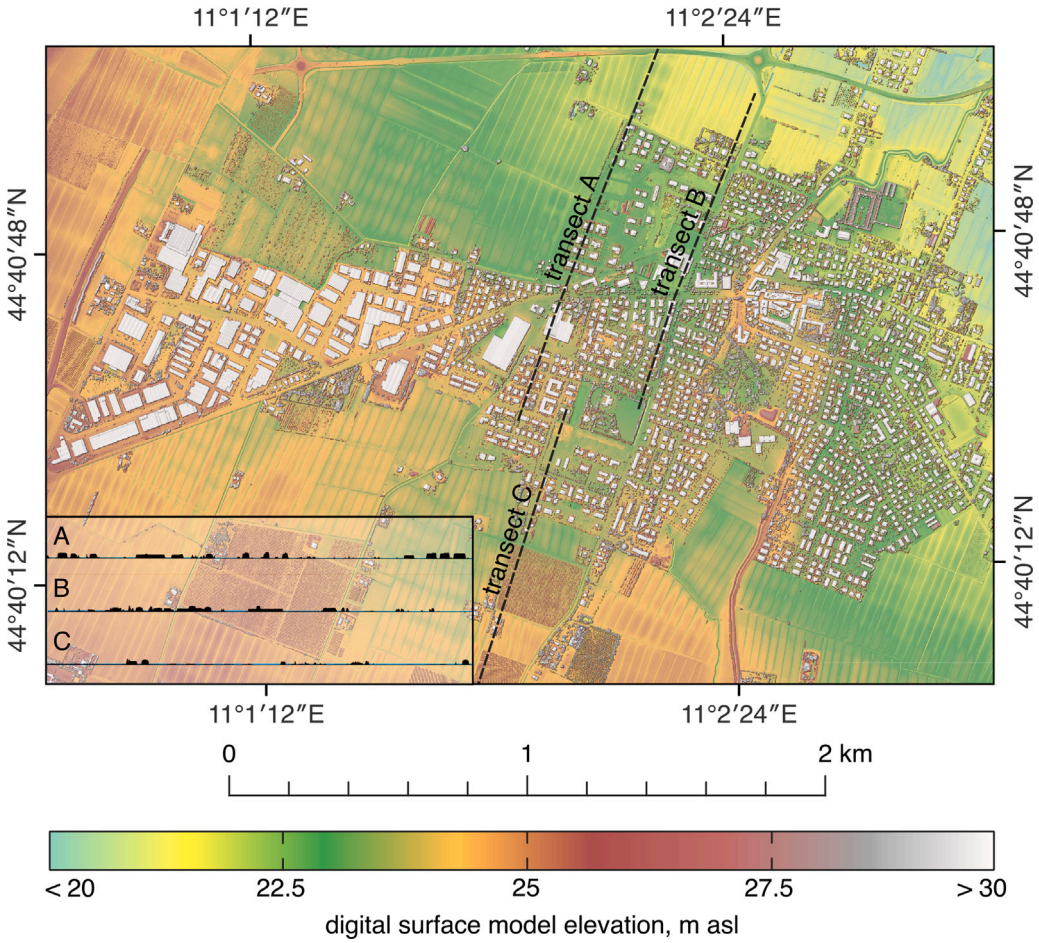

Fig. 12. Transects A, B, and C in the inset d of Fig. 1 along which the maximum water-surface elevation obtained by using digital terrain model (DTM) and digital surface model (DSM) data are compared (Fig. 13).

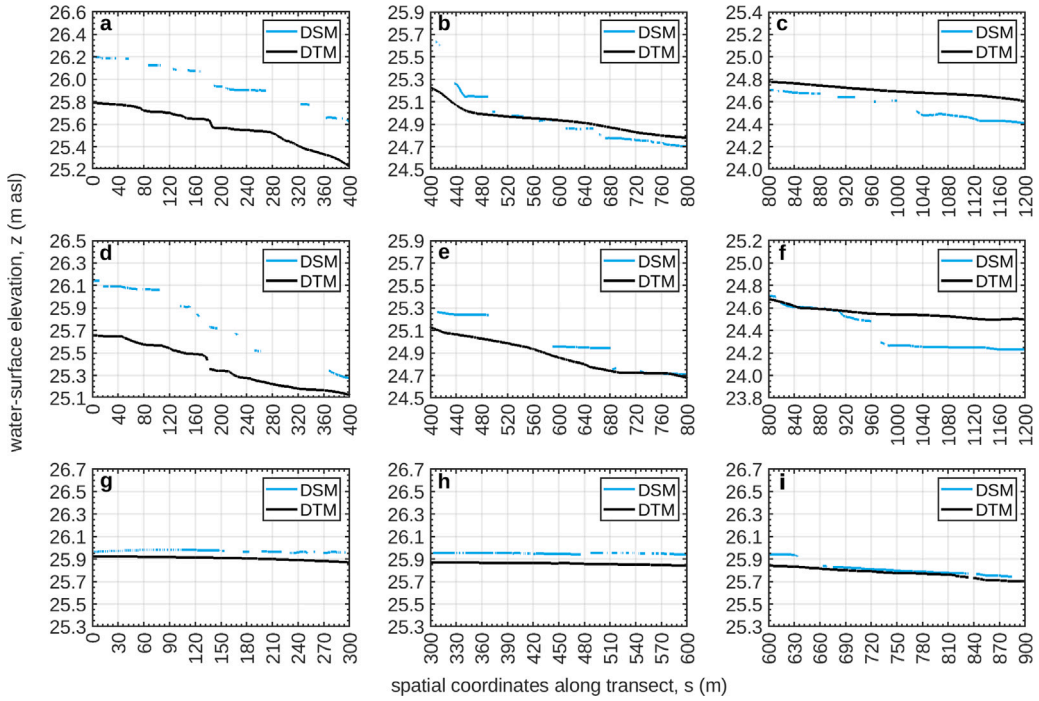

Fig. 13. Comparison between simulated maximum water-surface elevation along transects reported in Fig. 12 as obtained by using digital terrain model (DTM) or digital surface model (DSM) data and unstructured meshes based on LANDMARK with S_c equal to 10 m^2 and P_t equal to 0.25 m. Results obtained along transect A, B, and C in Fig. 12 are reported in plots (a, b, c), (d, e, f), and (g, h, i), respectively.

The comparison between type-1 and type-2 errors in predicted flood areas indicates the detail with which the ridge network needs to be extracted, the breaklines need to be identified, and the unstructured mesh for 2D flood inundation modeling needs to be generated. Having set $P_t = 0.25$ m in all cases, the detail in the representation of ridges is indicated in Fig. 10 by S_c. The lower is S_c, the higher is the detail of the extracted ridge network. The use of DSM data in preference to DTM data is found to reduce significantly both E_1 and E_2 when detailed ridge networks, breaklines, and unstructured computational meshes are used ($S_c \leq 10^3$ m^2, Figs. 4a–4c, 5a, and 5b). More specifically, one can note that using DSM data in preference to DTM data leads to a reduction of 42% in E_1 for $S_c = 10$ m^2 (Fig. 10a) and to a reduction of 36% in E_2 for $S_c = 10$ m^2 (Fig. 10b). Instead, E_1 and E_2 are smaller with DTM data than with DSM data when the detail of ridges, breaklines, and unstructured computational meshes is inadequate to represent macrostructures observed in DSM data ($S_c \geq 10^4$ m^2, Figs. 4e, 4f, 5a, and 5b). These results suggest that a profitable use of DSM data in preference to DTM data can only be achieved by using high-resolution DSM data (1-m DSM data in the present study), advanced terrain analysis methods (the LANDMARK algorithm in the present study), and flood inundation models (HEC-RAS 2D in the present study) that take advantages of high-resolution topographic data along the edges of computational mesh elements. With DSM data and/or terrain analysis methods that are inadequate to describe trees and buildings, the use of relatively smoother DTM data where topographic macrostructures are filtered out remains the best modeling strategy.

Negative lag times (ranging from −2.75 to −1.50 h in Tab. S1) and relative errors (ranging from −29% to −28% in Tab. S1) are systematically obtained when DTM data are used and this indicates that simulated flood inundations come in advance with respect to observed flood inundations as expected from neglecting the impact of land surface macrostructures on flood inundation dynamics (supporting information, Tab. S1). The explicit description of land surface macrostructures based on the use of DSM data reduces significantly lag times between simulated and observed times of arrival (equal to 0.25 h in Tab. S1) and the related relative errors (ranging from −5% to −3% in Tab. S1). The detail of the unstructured mesh based on DSM data significantly impacts the time of travel of the flood inundation (Fig. 11). In facts, the flood inundation reaches the South of Nonantola (inset in Fig. 11) about 5 h after the levee failure in the DSM-based flood inundation model with the finest computational mesh ($S_c = 10$ m^2, Fig. 11a), whereas it reaches the South of Nonantola about 2 h after the levee failure in the DSM-based flood inundation model with the coarsest computational mesh ($S_c = 10^6$ m^2, Fig. 11f). As shown in the insets of Fig. 11, the impact of topographic macrostructures on times of travel is especially relevant where natural or human-made barriers exist. Based on observed and simulated times of arrival for the real flood inundation event considered in this study the use of DSM data in preference to DTM data leads to a 25% improvement in the prediction of times of travel (supporting information, Fig. S7 and Tab. S1).

The comparison between water-surface elevations reported in Fig. 13 with reference to the transects A, B, and C shown in Fig. 12 reveals the conditions under which the use of DSM data in preference to DTM data is especially relevant. Along transect A, simulated water-surface elevations with DSM data are up to 0.40 m higher than those simulated with DTM data when urban areas are considered (Fig. 13a), whereas simulated water-surface elevations with DSM data are up 0.20 m lower than those simulated with DTM data when surface flow is released by urban areas to rural areas (Fig. 13c). A transition between the two different surface flow conditions occurs between urban and rural settings (Fig. 13b). Along transect B, a similar pattern is observed with higher water-surface elevations of about 0.43 m occurring in the urban area (Fig. 13d), lower water-surface elevations of about 0.23 m in the rural area (Fig. 13f), and a transition between the two different patterns at the interface between urban and rural areas (Fig. 13e). Along transect C, water-surface elevations simulated with DSM and DTM data are comparable because the terrain is everywhere rural along the transect and no significant macrotopographic structures are observed in DSM data (Figs. 13g, 13h, and 13i). The water profiles shown in Fig. 13 confirm that topographic macrostructures affect significantly surface flow depth by reducing flow velocity and increasing water-surface elevation. The use of DSM data seems therefore to be especially relevant to describe flood inundations in urban areas and at the interface between rural and urban areas.

5. Conclusions

This study showed that high-resolution digital surface model (DSM) data can be used to describe explicitly land surface macrostructures like trees and buildings in 2D flood inundation models (Section 2, Figs. 1, 3, and 5). Accuracy and computational efficiency are ensured by using the HEC-RAS 2D flood inundation model in combination with the LANDMARK terrain analysis algorithm (Sections 2.3 and 2.4, Figs. 6, 7, and 8). The impacts of geomorphologically-informed mesh (GIM) and geomorphologically-uninformed mesh (GUM) refinements in DSM and DTM data are evaluated by comparing simulated and observed flood areas over all the cases reported in Table 1. The obtained results indicate that, even under the simplifying assumption of impermeable macrostructures, especially when GIM refinement is applied, the use of DSM data in preference to DTM data leads to significant improvement in flood predictions (Fig. 9). The use of DSM data may not bring significant improvement over the traditional use of DTM data when unstructured meshes are insufficiently detailed to describe land surface macrostructures (Figs. 9 and 10).

For the real flood inundation event occurred in northern Italy in 2020, it is found that the explicit description of land surface macrostructures based on the combined use of a 1-m DSM, the LANDMARK terrain analysis algorithm, and the HEC-RAS 2D flood inundation model yields a 42% improvement in the prediction of flood area, a 36% improvement in the prediction of flood areal position, and a 25% improvement in the prediction of flood inundation time of travel with respect to the use of DTM data and resistance coefficients representing both land surface micro and macrostructures (Figs. 10 and 11). The direct use of DSM data in flood inundation models is particularly relevant within urban areas and at the interface between rural and urban areas (Figs. 12 and 13). The results obtained in this study clearly indicate the potential of using DSM data in combination with GIM refinement in flood inundation modeling, and are expected to apply to all those flood inundation models that make the same smart use of high-resolution topographic data as HEC-RAS 2D. The use of permeable macrostructures will be explored in future studies as a next logical step.

CRediT authorship contribution statement

Simone Pizzileo: Writing – review & editing, Writing – original draft, Validation, Software, Methodology, Investigation, Formal analysis, Conceptualization. **Giovanni Moretti:** Writing – review & editing, Writing – original draft, Validation, Software, Methodology, Investigation, Formal analysis, Conceptualization. **Stefano Orlandini:** Writing – review & editing, Writing – original draft, Validation, Software, Methodology, Investigation, Formal analysis, Conceptualization.

Declaration of competing interest

The authors declare the following financial interests/personal relationships which may be considered as potential competing interests: Stefano Orlandini reports financial support was provided by Fondazione Cassa di Risparmio di Modena. Stefano Orlandini reports financial support was provided by European Union NextGenerationEU NRRP Mission 4 Component 2. Stefano Orlandinireports financial support was provided by European Union NextGenerationEU NRRP PRIN 2022. If there are other authors, they declare that they have no known-competing financial interests or personal relationships that could have appeared to influence the work reported in this paper.

Data availability

Data will be made available on request.

Acknowledgments

The research reported in the present paper was supported by Fondazione Cassa di Risparmio di Modena through the grant 2018-0093, by the University of Modena and Reggio Emilia through the grant FAR 2020 Mission Oriented, by the European Union NextGenerationEU/NRRP, Mission 4 Component 2 Investment 1.5, Call 3277 (12/30/2021), Award 0001052 (06/23/2022), under the project ECS00000033 "Ecosystem for Sustainable Transition in Emilia-Romagna", Spoke 6 "Ecological Transition Based on HPC and Data Technology", and by the European Union NextGenerationEU/NRRP under the PRIN 2022 project 2022M4798K "Rivers Affected by Mammal Bioerosion". High-resolution topographic data were provided by "Ministero dell'Ambiente, della Tutela del Territorio e del Mare" (Rome, Italy), "Agenzia Interregionale per il Fiume Po" (Parma, Italy), and "Regione Emilia-Romagna" (Bologna, Italy). The observations of the flood event occurred along the Po Valley flood plain on 6 December 2020 were provided by "Protezione Civile della Regione Emilia-Romagna" (Italy), by "Corpo Nazionale dei Vigili del Fuoco" (Modena, Italy), and by "Consorzio della Bonifica Burana" (Modena, Italy). The term "geomorphologically-informed mesh (GIM)" was suggested by Efi Foufoula-Georgiou. The authors thank the Editor Gabriele Villarini, Brett Sanders, an anonymous reviewer, and Rachit Soni for comments that led to improvements in the manuscript.

Appendix A. Supplementary data

Supplementary material related to this article can be found online at https://doi.org/10.1016/j.advwatres.2024.104713.

References

Aristizabal, F., Salas, F., Petrochenkov, G., Grout, T., Avant, B., Bates, B., Spies, R., Chadwick, N., Wills, Z., Judge, J., 2023. Extending height above nearest drainage to model multiple fluvial sources in flood inundation mapping applications for the U.S. national water model. Water Resour. Res. 59, http://dx.doi.org/10.1029/2022WR032039, e2022WR032039.

Azizian, A., Brocca, L., 2020. Determining the best remotely sensed DEM for flood inundation mapping in data sparse regions. Int. J. Remote Sens. 41, 1884–1906. http://dx.doi.org/10.1080/01431161.2019.1677968.

Bates, P.D., De Roo, A.P., 2000. A simple raster-based model for flood inundation simulation. J. Hydrol. 236, 54–77. http://dx.doi.org/10.1016/S0022-1694(00)00278-X.

Bates, P.D., Marks, K.J., Horritt, M.S., 2003. Optimal use of high-resolution topographic data in flood inundation models. Hydrol. Process. 17, 537–557. http://dx.doi.org/10.1002/hyp.1113.

Bedient, P.B., Huber, W.C., Vieux, B.E., 2013. Hydrology and Floodplain Analysis, fifth ed. Pearson, London.

Begnudelli, L., Sanders, B.F., 2007. Simulation of the St. Francis dam-break flood. J. Eng. Mech. 133, 1200–1212. http://dx.doi.org/10.1061/(ASCE)0733-9399(2007)133:11(1200).

Brandimarte, L., Woldeyes, M.K., 2013. Uncertainty in the estimation of backwater effects at bridge crossings. Hydrol. Process. 27, 1292–1300. http://dx.doi.org/10.1002/hyp.9350.

Camporese, M., Paniconi, C., Putti, M., Orlandini, S., 2010. Surface-subsurface flow modeling with path-based runoff routing, boundary condition-based coupling, and assimilation of multisource observation data. Water Resour. Res. 46, W02512. http://dx.doi.org/10.1029/2008WR007536.

Casas, A., Benito, G., Thorndycraft, V., Rico, M., 2006. The topographic data source of digital terrain models as a key element in the accuracy of hydraulic flood modelling. Earth Surf. Process. Landf. 31, 444–456. http://dx.doi.org/10.1002/esp.1278.

Chaudhuri, C., Gray, A., Robertson, C., 2021. InundatEd-v1.0: A height above nearest drainage HAND-based flood risk modeling system using a discrete global grid system. Geosci. Model Dev. 14, 3295–3315. http://dx.doi.org/10.5194/gmd-14-3295-2021.

Chow, V.T., 1959. Open-Channel Hydraulics. McGraw-Hill, New York.

Chow, V.T., Maidment, D.R., Mays, L.W., 1988. Applied Hydrology. McGraw-Hill, New York.

Costabile, P., Macchione, F., 2015. Enhancing river model set-up for 2D dynamic flood modelling. Environ. Model. Softw. 67, 89–107. http://dx.doi.org/10.1016/j.envsoft.2015.01.009.

Di Martire, D., Paci, M., Confuorto, P., Costabile, S., Guastaferro, F., Verta, A., Calcaterra, D., 2017. A nation-wide system for landslide mapping and risk management in Italy: The second not-ordinary plan of environmental remote sensing. Int. J. Appl. Earth Obs. Geoinf. 63, 143–157. http://dx.doi.org/10.1016/j.jag.2017.07.018.

Dottori, F., Di Baldassarre, G., Todini, E., 2013. Detailed data is welcome, but with a pinch of salt: Accuracy, precision, and uncertainty in flood inundation modeling. Water Resour. Res. 49, 6079–6085. http://dx.doi.org/10.1002/wrcr.20406.

Garousi-Nejad, I., Tarboton, D.G., Aboutalebi, M., Torres-Rua, A., 2019. Terrain analysis enhancements to the height above nearest drainage flood inundation mapping method. Water Resour. Res. 55, 7983–8009. http://dx.doi.org/10.1029/2019WR024837.

Ghanghas, A., Dey, S., Merwade, V., 2022. Evaluating the reliability of synthetic rating curves for continental scale flood mapping. J. Hydrol. 606, 127470. http://dx.doi.org/10.1016/j.jhydrol.2022.127470.

Guinot, V., Sanders, B.F., Schubert, J.E., 2017. Dual integral porosity shallow water model for Urban flood modelling. Adv. Water Resour. 103, 16–31. http://dx.doi.org/10.1016/j.advwatres.2017.02.009.

Guth, P.L., 2006. Geomorphometry from SRTM: Comparison to NED. Photogramm. Eng. Remote Sens. 72, 269–277. http://dx.doi.org/10.14358/PERS.72.3.269.

Harvey, A., 2022. Introducing geomorphology. In: Introducing Earth and Environmental Sciences. Dunedin Academic Press, Edinburgh.

Hocini, N., Payrastre, O., Bourgin, F., Gaume, E., Davy, P., Lague, D., Poinsignon, L., Pons, F., 2021. Performance of automated methods for flash flood inundation mapping: A comparison of a digital Terrain model (DTM) filling and two hydrodynamic methods. Hydrol. Earth Syst. Sci. 25, 2979–2995. http://dx.doi.org/10.5194/hess-25-2979-2021.

Horritt, M.S., Bates, P.D., 2001. Effects of spatial resolution on a raster based model of flood flow. J. Hydrol. 253, 239–249. http://dx.doi.org/10.1016/S0022-1694(01)00490-5.

Hydrologic Engineering Center, 2016. HEC-RAS: River analysis system. In: Hydraulic Reference Manual. US Army Corps of Engineers Hydrologic Engineering Center, Davis, CA.

Hydrologic Engineering Center, 2020a. HEC-RAS 2D user's manual. In: Hydraulic Reference Manual. US Army Corps of Engineers Hydrologic Engineering Center, Davis, CA.

Hydrologic Engineering Center, 2020b. Modeler application guidance for steady vs unsteady, and 1D vs 2D vs 3D hydraulic modeling. In: Training Document. US Army Corps of Engineers Hydrologic Engineering Center, Davis, CA.

Hydrologic Engineering Center, 2022. Development of the 2D computational mesh. In: Training Document. US Army Corps of Engineers Hydrologic Engineering Center, Davis, CA.

Kahl, D.T., Schubert, J.E., Jong-Levinger, A., Sanders, B.F., 2022. Grid edge classification method to enhance levee resolution in dual-grid flood inundation models. Adv. Water Resour. 168, 104287. http://dx.doi.org/10.1016/j.advwatres.2022.104287.

Katul, G.G., Poggi, D., Ridolfi, L., 2011. A flow resistance model for assessing the impact of vegetation on flood routing mechanics. Water Resour. Res. 47 (W08533), http://dx.doi.org/10.1029/2010WR010278.

Katul, G.G., Wiberg, P., Albertson, J., Hornberger, G., 2002. A mixing layer theory for flow resistance in shallow streams. Water Resour. Res. 38, 32–1–32–8. http://dx.doi.org/10.1029/2001WR000817.

Kim, J., Ivanov, V.Y., Katopodes, N.D., 2012. Hydraulic resistance to overland flow on surfaces with partially submerged vegetation. Water Resour. Res. 48 (W10540), http://dx.doi.org/10.1029/2012WR012047.

Kim, B., Sanders, B.F., Famiglietti, J.S., Guinot, V., 2015. Urban flood modeling with porous shallow-water equations: A case study of model errors in the presence of anisotropic porosity. J. Hydrol. 523, 680–692. http://dx.doi.org/10.1016/j.jhydrol.2015.01.059.

Leopold, L.B., Wolman, M.G., Miller, J.P., 1964. In: Freeman, W.H. (Ed.), Fluvial Processes in Geomorphology. San Francisco, CA, USA.

Li, Z., Mount, J., Demir, I., 2022. Accounting for uncertainty in real-time flood inundation mapping using hand model: Iowa case study. Nat. Hazards 112, 977–1004. http://dx.doi.org/10.1007/s11069-022-05215-z.

Liang, D., Falconer, R.A., Lin, B., 2007. Coupling surface and subsurface flows in a depth averaged flood wave model. J. Hydrol. 337, 147–158. http://dx.doi.org/10.1016/j.jhydrol.2007.01.045.

Longley, P., 2005. Geographical information systems: Principles, techniques. In: Management and Applications. Wiley, New York.

Marks, K., Bates, P.D., 2000. Integration of high-resolution topographic data with floodplain flow models. Hydrol. Process. 14, 2109–2122. http://dx.doi.org/10.1002/1099-1085(20000815/30)14:11/12%3C2109::AID-HYP58%3E3.0.CO;2-1.

Mason, D.C., Cobby, D.M., Horritt, M.S., Bates, P.D., 2003. Floodplain friction parameterization in two-dimensional river flood models using vegetation heights derived from airborne scanning laser altimetry. Hydrol. Process. 17, 1711–1732. http://dx.doi.org/10.1002/hyp.1270.

Mays, L.W., 2010. Water Resources Engineering. John Wiley and Sons, New York.

Medeiros, S.C., Bobinsky, J.S., Abdelwahab, K., 2022. Locality of topographic ground truth data for salt marsh Lidar DEM elevation bias mitigation. IEEE J. Sel. Top. Appl. Earth Obs. Remote Sens. 15, 5766–5775. http://dx.doi.org/10.1109/JSTARS.2022.3189226.

Merz, B., Kreibich, H., Schwarze, R., Thieken, A.H., 2010. Review article assessment of economic flood damage. Nat. Hazards Earth Syst. Sci. 10, 1697–1724. http://dx.doi.org/10.5194/nhess-10-1697-2010.

Moretti, G., Orlandini, S., 2008. Automatic delineation of drainage basins from contour elevation data using skeleton construction techniques. Water Resour. Res. 44 (W05403), http://dx.doi.org/10.1029/2007WR006309.

Moretti, G., Orlandini, S., 2023. Thalweg and ridge network extraction from unaltered topographic data as a basis for Terrain partitioning. J. Geophys. Res.: Earth Surf. 128, http://dx.doi.org/10.1029/2022JF006943, e2022JF006943.

National Academies of Sciences, Engineering, and Medicine, 2024. Selection and Application of Manningś Roughness Values in Two-Dimensional Hydraulic Models. NCHRP Research Report 1077, The National Academies Press, Washington, DC, http://dx.doi.org/10.17226/27730.

Orlandini, S., Moretti, G., Albertson, J.D., 2015. Evidence of an emerging levee failure mechanism causing disastrous floods in Italy. Water Resour. Res. 51, 7995–8011. http://dx.doi.org/10.1002/2015WR017426.

Pappenberger, F., Matgen, P., Beven, K.J., Henry, J.B., Pfister, L., Fraipont, P., 2006. Influence of uncertain boundary conditions and model structure on flood inundation predictions. Adv. Water Resour. 29, 1430–1449. http://dx.doi.org/10.1016/j.advwatres.2005.11.012.

Parker, D.J., 2017. Flood Warning Systems and their Performance. Oxford Research Encyclopedia of Natural Hazard Science, http://dx.doi.org/10.1093/acrefore/9780199389407.013.84.

Petrie, G., Kennie, T.J.M., 1987. Terrain modelling in surveying and civil engineering. Comput. Aided Des. 19, 171–187. http://dx.doi.org/10.1016/0010-4485(87)90066-2.

Sanders, B.F., 2007. Evaluation of on-line DEMs for flood inundation modeling. Adv. Water Resour. 30, 1831–1843. http://dx.doi.org/10.1016/j.advwatres.2007.02.005.

Sanders, B.F., Mrše, R.D., 2007. Resistance to flooding by mega-roughness. In: Proceedings of the 32nd Congress of IAHR. Venice, Italy.

Sanders, B.F., Schubert, J.E., Gallegos, H.A., 2008. Integral formulation of shallow-water equations with anisotropic porosity for Urban flood modeling. J. Hydrol. 362, 19–38. http://dx.doi.org/10.1016/j.jhydrol.2008.08.009.

Sanders, B.F., Schubert, J.E., Goodrich, K.A., Houston, D., Feldman, D.L., Basolo, V., Luke, A., Boudreau, D., Karlin, B., Cheung, W., Contreras, S., Reyes, A., Eguiarte, A., Serrano, K., Allaire, M., Moftakhari, H., AghaKouchak, A., Matthew, R.A., 2020. Collaborative modeling with fine-resolution data enhances flood awareness, minimizes differences in flood perception, and produces actionable flood maps. Earth's Fut. 8, http://dx.doi.org/10.1029/2019EF001391, e2019EF001391.

Schubert, J.E., Sanders, B.F., 2012. Building treatments for Urban flood inundation models and implications for predictive skill and modeling efficiency. Adv. Water Resour. 41, 49–64. http://dx.doi.org/10.1016/j.advwatres.2012.02.012.

Schubert, J.E., Sanders, B.F., Smith, M.J., Wright, N.G., 2008. Unstructured mesh generation and landcover-based resistance for hydrodynamic modeling of Urban flooding. Adv. Water Resour. 31, 1603–1621. http://dx.doi.org/10.1016/j.advwatres.2008.07.012.

Tsubaki, R., Fujita, I., 2010. Unstructured grid generation using Lidar data for Urban flood inundation modelling. Hydrol. Process. 24, 1404–1420. http://dx.doi.org/10.1002/hyp.7608.

Wang, L., Cui, S., Tang, J., Fang, L., Fang, X., Shrestha, S., Manandhar, B., Huang, J., Nitivattananon, V., 2023. Riverine flood risk assessment with a combined model chain in southeastern China. Ecol. Indic. 154, 110686. http://dx.doi.org/10.1016/j.ecolind.2023.110686.

Yu, D., Lane, S., 2006a. Urban fluvial flood modelling using a two-dimensional diffusion-wave treatment, part 1: Mesh resolution effects. Hydrol. Process. 20, 1541–1565. http://dx.doi.org/10.1002/hyp.5935.

Yu, D., Lane, S., 2006b. Urban fluvial flood modelling using a two-dimensional diffusion-wave treatment, part 2: Development of a sub-grid-scale treatment. Hydrol. Process. 20, 1567–1583. http://dx.doi.org/10.1002/hyp.5936.